SCANNING ELECTROCHEMICAL MICROSCOPY CHARACTERIZATION OF SOL-GEL COATINGS APPLIED ON AA2024-T3 SUBSTRATE FOR CORROSION PROTECTION

Diógenes J. Carbonell[1], Amaya García-Casas[1], Javier Izquierdo[2,3], Ricardo M. Souto[2,3], Juan Carlos Galván[4], Antonia Jiménez-Morales[1]

[1] Departamento de Ciencia e Ingeniería de Materiales e Ingeniería Química, Universidad Carlos III de Madrid, Avda. Universidad 30, 28911 Leganés, Madrid, Spain.

[2] Department of Chemistry, Universidad de La Laguna, Avda. Astrofísico Francisco Sánchez s/n, 38206 La Laguna, Tenerife, Spain.

[3] Institute of Material Science and Nanotechnology, Universidad de La Laguna, 38200 La Laguna, Tenerife, Spain.

[4] Centro Nacional Investigaciones Metalúrgicas, CSIC, 28040 Madrid, Spain.

Abstract

Scanning electrochemical microscopy was employed to characterize the local surface activity of an AA2024-T3 coated with sol-gel. Corrosion inhibitors were added to the sol-gel either as soluble chemical species, namely 1,2,3-benzotriazole, Na-(diethyl(dithiocarbamate)), and piperazine, or using Ce(III)-montmorillonite containers. The Scanning electrochemical microscopy was operated in the feedback mode by using ferrocene-methanol as redox mediator. This experimental procedure allowed evaluation of the coating behaviour in damaged and non-damaged areas from the analysis of *Z*-approach curves and 2D maps. The results evidence differences in the local electrochemical activity of the modified coatings that correlate well with averaging electrochemical measurements using electrochemical impedance spectroscopy.

Keywords: Aluminium Alloy; Interfaces; Polymer coatings; Scanning electrochemical microscopy; EIS.

1. Introduction

Aluminium alloys from the 2xxx series, which contains copper and magnesium as main alloying elements, are widely used in the aerospace industry due to their low density and good mechanical properties [1]. However, these materials lack sufficient corrosion resistance in aggressive saline environments because of the inherent inhomogeneous distribution of the intermetallic particles across the surface [2,3]. In order to protect these alloys against corrosion, the sol-gel technology has been investigated as a potential alternative to chromium-based protection methods, due to low temperature processing, tailored design, and formation of dense and homogenous Cr(VI)-free-coatings [4-6].

There are several organo-inorganic hybrid materials, such as γ-methacryloxypropyltrimethoxysilane (MAPTMS) and tetramethylorthosilicate (TMOS), which have been employed as precursors for sol-gel coatings applied on aluminium alloys [7]. The sol-gel technology creates a network that can accommodate different substances that may effectively improve the corrosion protection performance of materials. On the basis of the corrosion protection effect exerted by these substances added to the sol-gel coating, we can distinguish between inhibitors and cross-linking agents. A range of compounds has been proved to inhibit corrosion on aluminium alloys in chloride containing electrolytes, including benzotriazole (BTZ) and Na-(diethyl(dithiocarbamate)) (DDCT), but they have not yet been characterized when added into a sol-gel matrix [8]. On the other hand, piperazine (PIP) has been regarded to be an effective cross-linking promoter for sol-gel treatments when added to the aqueous solution. This effect is due to the creation of a 3D network that acts as a physical barrier, thus hindering corrosion reactions [9]. Furthermore, several cerium-based compounds have also been reported to exhibit inhibitor properties against electrochemical corrosion [10-12].

Sol-gel coatings on metallic substrates are often characterized by Electrochemical Impedance Spectroscopy (EIS) in order to quantify their barrier properties in an aggressive electrolyte. [13,14]. Yet, aluminium alloys are well-known to suffer from localized corrosion in aggressive saline environment [2,3], whereas EIS provides only general information because it averages the current response originated from the complete exposed surface. Therefore, this technique does not adequately resolve local effects contributing to the mechanism of the corrosion process. For that purpose, the Scanning Electrochemical Microscopy (SECM) technique, which makes use of an ultramicroelectrode (UME) to raster the substrate in a given electrolyte [15], is regarded suitable because it allows acquisition of spatially-resolved electrochemical information in close vicinity of a heterogeneous electroactive surface. The characterization of corroding surfaces with the

conventional amperometric operation modes of the SECM involves the analysis and evaluation of the redox reactions that an electrochemically active species, present in the diffusion layer of the liquid-solid interface in the substrate surface, may undergo either at the UME or at the (in)homogeneous substrate. These species may (heterogeneously) originate from the substrate, or be (un)intentionally added to the test solution, and their concentration can experience changes due to either diffusion in the electrolyte or electrochemical interaction with the UME and the substrate. SECM has been successfully employed to monitor the formation of inhibitor films on reactive metals [16-22], the degradation mechanisms of organic films [23-29] and surface coatings applied on different metals [30-34], and the detection of the electrochemical reactions occurring at defects of coated metals [35-38].

The strategy investigated here is to encapsulate different substances with potential activity to enhance the corrosion protection of sol-gel coatings applied on 2024-T3 aluminium alloy. The investigated additives are: (1) an inhibitor substance (BTZ and DDTC), (2) a cross-linking agent (PIP), and (3) a substance that is expected to operate with both corrosion protection mechanisms, namely a Ce(III)-montmorillonite (CeMMT). The differences between the four coatings and the influence of the various substances encapsulated into the sol-gel coatings was studied by SECM, and results were compared with the spatially-resolved results obtained using EIS. In this paper we demonstrate that this multiscale electrochemical characterization procedure assists to screen differences in the corrosion resistance of the different sol-gel coatings, and can be employed to determine the most efficient treatment to enhance the corrosion protection of the 2024-T3 aluminium alloy.

2. Experimental

2.1 Materials and sample preparation

The metallic substrates were panels of 2024-T3 aluminium alloy of thickness 3 mm. The panels were ground with silicon carbide paper of 1000 grit, and then polished using an alumina suspension in ultrapure deionised water and finished with a 3 μm alumina paste. Finally, the panels were cleaned with acetone in an ultrasonic bath.

Sols were prepared starting from a mixture of 4 mol of γ-methacryloxypropyltrimethoxysilane (MAPTMS, 98% from Aldrich) and 1 mol of tetramethylorthosilicate (TMOS, 98% from Fluka). Ethanol and water were added with the molar ratio silane/ethanol/water 1/3/3 [39]. A solution without phase separation and completely hydrolysed was obtained after 4 hours as described elsewhere [39]. After the hydrolysis, the sol solution was

placed in an oven at 60 ºC for 2 h until the viscosity of the solution was such that it was adequate to coat the aluminium panels by dip-coating. A viscosity of 10^{-2} Pa s is required to properly cover the aluminium parts with the sol-gel product.

Thirteen different sol-gel coatings were produced as listed in **Table 1**. All the species were mixed after the hydrolysis step and stirred for 5 min. Benzotriazole (BTZ), Na-(diethyl(ditiocarbamate)) (DDTC), and piperazine (PIP) were used as received from Aldrich Chemical. Ce(III)–montmorillonite (Ce-MMT) was prepared through an ion-exchange reaction, as it is described elsewhere [40]. Depending on the amount of inhibitor employed in the additions, the treated samples were classified as Low (LQ), Medium (MQ) and High (HQ) inhibitor content, respectively. Immediately after stirring the sol-gel mixed with the corresponding compound, the protective layer was applied to the samples simply by dipping them into the solutions for 100 s, followed with a withdrawal stage with a speed of 100 mm min^{-1}. After coating application, the samples were dried at room temperature for 30 min, followed by thermal treatment at 120 °C for 2 h inside an oven.

2.2 Instruments

Electrochemical impedance spectroscopy (EIS) measurements were performed in the conventional three-electrode cell arrangement, using an Ag/AgCl/KCl (3M) electrode as reference (E^0 = +0. 210 V vs. NHE), and a platinum wire as counter electrode. A surface area of 0.63 cm^2 of the working electrode was exposed to the test electrolyte. Impedance spectra were recorded using an Autolab PGSTAT302N potentiostat/galvanostat (Ecochemie, Utrecht, The Netherlands). The cell was placed in a Faraday cage to avoid external interferences from electromagnetic fields and wandering currents. Upon immersion in naturally-aerated 0.05 M NaCl solution at ambient temperature (20.5 ºC ± 2 ºC), the samples were left unpolarized for 1 h to spontaneously attain a stable Open Circuit Potential (OCP) in the test solution. Impedance measurements were subsequently performed at regular intervals for 72 h using an AC amplitude of 10 mV with respect to OCP, and a frequency scan ranging from 10 kHz to 10 mHz, the values spaced logarithmically with 10 points per decade. OCP was recorded for 10 minutes before and after each impedance measurement in order to monitor the stability of the coatings. EIS data were fitted and analyzed in terms of equivalent circuits (EC) using *ZView* software (Scribner Associates, Charlottesville, VA, USA) to obtain the relevant impedance parameters.

SECM experiments were carried out using a scanning electrochemical microscope built by Sensolytics (Bochum, Germany). Platinum ultramicroelectrodes (UME) were fabricated by sealing a

12.5 µm Pt wire in a glass capillary (inner diameter 1.125 mm, outer diameter 1.5 mm) pulled at the end [41]. This resulted in electrodes with a 12.5 µm diameter Pt microdisc insulated in glass. Electrodes were polished with 0.3 µm alumina water suspension prior to measurements in order to remove any fouling. SECM experiments were conducted in the three-electrode configuration with the Pt UME connected as working electrode, an Ag/AgCl/KCl (3M) as reference electrode, and a platinum ring as counter-electrode. The applied tip potential (+0.5 V vs. Ag/AgCl/KCl (3M)) corresponds to the oxidation of this complex to its ferrocenium form under diffusion-controlled conditions.

The as-prepared aluminium samples were mounted facing up in the SECM setup by using a sandwich-type cell, with a 2 cm diameter o-ring limiting the total exposed area. As an experimental procedure, the surface of the sample was first externally polarized at -1.4 V vs. Ag/AgCl/KCl (3M) in a 5 mM NaCl solution for 30 min inside the cell. After this polarization step, the electrolyte was removed and the sample was repositioned in the electrochemical cell in a way that both a portion of the pre-polarized surface region and a portion of the unmodified surface could be simultaneously exposed to 5 mM NaCl + 0.5 mM ferrocenemethanol, the latter employed as redox mediator. In this way, differences in the electrochemical reactivity of the surface between prior polarized and non-polarized surface regions could be detected by SECM operated in the feedback-mode. By recording the current measured at the Pt probe as it approached the surface (i.e., *Z*-approach curves, PAC), two over each of the regions defined on the surface of the material, the substrate-coating systems could be tested by comparing the behaviours obtained over non- and previously-polarized areas. The curves were recorded at constant approximation rate of 1 µm s^{-1}, starting from the bulk of the solution. Tip-current values in this work have been normalized by dividing them by the measured limiting current, $I_{t,\infty}$. The tip was approached towards the surface until the negative feedback effect was affected by the unavoidable imperfect planar geometry of the insulating glass surrounding the microdisc, which contacts the surface and therefore prevents the metallic microdisc might reach smaller tip-substrate distances. This situation was evidenced by a change in the slope (turning point) after which the tip current barely decreases while the SECM motor is still moving and pushing the probe down towards the sample. This point was taken as $Z = 0$, and distances relative to this point were used for plotting.

3 Results and discussion

The barrier properties provided to 2024-T3 aluminium alloy by applying sol-gel protective coatings with different loads of inhibitors was investigated using both conventional averaging

electrochemical techniques, namely electrochemical impedance spectroscopy (EIS), and the scanning electrochemical microscope (SECM). Characterization was performed by immersing the samples in naturally-aerated aqueous solution containing NaCl, without the application of any external polarization to them, thus effectively at their corresponding open circuit potential (OCP). Whereas EIS data provide an averaging description of the exposed surface, SECM provides spatially-resolved information on any eventual chemical heterogeneity present on the surface while operated in the feedback mode using ferrocene-methanol as redox mediator. The latter could originate from the actual sol-gel coating process and it was imaged as 2D maps, or by originating two different regions on a given sample by the operator, that could be distinguished from recording *Z*-approach curves.

3.1 Electrochemical characterization: barrier properties

Information on the barrier properties of sol-gel coated 2024-T3 aluminium alloy was derived from electrochemical impedance spectra recorded at their corresponding open circuit potential (OCP) after 72 hour immersion in 0.05 M NaCl solution. Both non-doped (taken as control), and the doped coatings of various compositions listed in **Table 1**, were characterized in this way. The stability of the OCP during the measurements was established by monitoring their time evolution up to 72 hours exposure, and they are given in **Table 2**. Differences between the starting and final OCP values remained smaller than 50 mV in all cases.

The control coating was first considered in order to take it as reference. The EIS data of the control coating are depicted in **Figure 1** in the form of Nyquist (complex versus real components of the impedance) and Bode (impedance modulus and phase angle versus frequency) plots. Two time constants are observed in the spectrum, and they could be satisfactorily fitted using the equivalent circuit shown in **Figure 2A**, which describes the barrier characteristics of an unsealed inhomogeneous film [42]. It assumes that the corrosion resistance of the material is provided by a bilayer barrier film composed by a thin internal layer of native oxide, and an unsealed outer layer due to the silane contribution, in agreement with previous reports [43-46]. The following elements are considered: R_s represents the uncompensated resistance of the test electrolyte; the high frequency time constant, R_f C_f is associated to the barrier characteristics of the silane film, whereas the time constant at lower frequencies, R_o C_o corresponds to the pore resistance and the capacitance of the oxide/hydroxide alumina film. A finite element Warburg (W) was added in order to account for a diffusional process. The good agreement between fitted and measured data is shown in **Figure 1**, with a chi-square value smaller than 10^{-3}.

A constant phase element (CPE) was employed to take into account the intrinsic inhomogeneities of the oxidized metal surface, and they are described by:

$$Z_{(CPE)} = \frac{1}{Y_0\ (j\omega)^n} \qquad (1)$$

where ω is the angular frequency and Y_0 is a constant, and the value of the exponent n indicates the deviation from ideal capacitive behaviour (e.g., when n = 1). From the CPE parameters, capacitance values were derived using [47]:

$$C = \left(R^{1-n}Q\right)^{1/n} \qquad (2)$$

Accordingly, the calculated value of the capacitance of the silane film is C_f = 1.62 μF cm^{-2}. This value allows the film thickness to be estimated assuming the parallel plate capacitance approximation:

$$C_f = \frac{\varepsilon\varepsilon_0}{d} \qquad (3)$$

where ε_0 = 8.85×10^{-10} F cm^{-1}; ε is the permittivity of the coating, which is assumed to be 2 [48]; and d is the thickness of the coating. This calculation gave 10.9 μm for the coating thickness, which is bigger than the values previously determined from cross-section SEM images when this sol-gel coating system was applied on Mg-Al alloys instead [7]. However, this value is in good agreement with the thickness determined with a cross section of each material by Scanning Electrochemical Microscopy (SEM). The thickness ranged from 7 to 15 μm. **Figure 3** shows the cross section of the control coating as representative for all the coatings prepared. On the other hand, it must also be noticed that the film resistance of the inhibitor-free coating is rather poor (cf. **Table 2**), which is critical regarding the anticorrosive properties of the coated 2024-T3 aluminium alloy.

Modification of corrosion protective characteristics of sol-gel coated 2024-T3 alloy with additions of benzotriazole (BTZ), Na-(diethyl(dithiocarbamate)) (DDTC), piperazine (PIP) and Ce(III)-montmorillonite (CeMMT) was investigated by EIS, and the obtained impedance spectra are given in **Figure 4**. Therefore, it can be regarded that the electrochemical behaviour of the modified sol-gel coatings is mainly determined by the silane layer itself. Yet, some distinctive features must be taken into account, namely (1) the occurrence of higher resistance values in high and low frequency limits of the Bode-magnitude diagrams, which are greatly affected by the nature and concentration of the additions to the sol-gel; and (2) the shift of the frequency at which the maximum phase angle is observed at intermediate frequencies, in most cases towards smaller frequency values except for benzotriazole. Therefore, the various additions to the sol-gel provide some increased corrosion resistance to the coated 2024-T3 aluminium alloy, though to a different extent. From a cursory

inspection of both Nyquist and Bode diagrams it can be observed three different behaviours. (1) Coatings modified with BTZ, DDTC, CeMMT-LQ and CeMMT-MQ presented a very similar shape to the one obtained with the control (inhibitor-free coating). Two time constants are found again for all these systems, and therefore impedance analysis can be performed using the equivalent circuit displayed in **Figure 2A** to obtain the parameters listed in **Table 2. (**2) Coatings modified with CeMMT-HQ, PIP-LQ and PIP-MQ presented also two time constants but their maximum angle and their impedance modulus in Bode plots shifted to lower frequencies and higher values, respectively. Hence, these coating showed better barrier properties in comparison with the first set of coatings. For the second set of coatings a similar equivalent circuit was used but a CPE was used at medium-high frequencies instead of a capacitor (**Figure 2B**). And, (3) the coating modified with high quantities of PIP is less satisfactorily described by the equivalent circuits previously proposed because an additional third time constant would be expected from the inspection of the corresponding Bode plot (**Figure 4L**). That is, additional impedance parameters R_3 and C_3 would be required to improve the fit quality. Though the introduction of a third constant to model the impedance spectra for sol-gel coatings applied on aluminium can be already found in the literature, this new time constant has been exclusively attributed to two alternate sources, namely (1) the development of large pores through the coating, resulting in more porous and less protective films [49-51], and (2) the effect of immersion time in the test environment, leading to coating degradation and the onset of the corrosion process at the buried metal, sometimes accompanied by eventual precipitation of corrosion products [52-54]. In both situations, less resistant coatings were thus found. But the opposite situation is observed in our case, because the PIP-HQ system exhibits the highest corrosion resistance among the tested doped and undoped silane coated aluminium alloys as it is readily observable from the inspection of the corresponding Nyquist and Bode plots given in Figures 1 and 4. Therefore, an alternate interpretation must be provided to justify the occurrence of a third time constant in the impedance spectra for this system, but it would require to consider this silane coating to be actually constituted by a bilayer, analogously to the behaviour of TiO_2 coatings prepared by sol-gel method [55]. Accordingly, the pair of R_f and C_f denote exclusively the resistance and capacitance of the inner silane coating, whereas R_3 and C_3 are the resistance and the capacitance of the outer porous silane coating. Unfortunately, though the bilayer structure of TiO_2 layers has been convincingly demonstrated using a combination of electrochemical and surface characterization techniques [56,57], no similar evidences are currently available in the case of a silane layer, and therefore a three-time constants model should not be adopted at this stage exclusively on the basis of a smaller chi-square value. From the foregoing, differences in the corrosion resistance of the modified coatings

from electrochemical impedance data has been preformed in terms of the equivalent circuit depicted in Figure 2B, as to determine the relative efficiencies of each treatment.

Addition of benzotriazole to the silane layer produces a weak effect on the corrosion protection characteristics of the coated aluminium alloy. In fact, the characteristics of the oxide/metal interface remain almost invariant compared to those determined for the undoped coating, as evidenced by the similar values of the pore resistance R_o and the capacitance C_o of the oxide/hydroxide alumina film, and the finite element Warburg (W). Therefore, the enhanced corrosion protection due to benzotriazole additions originates (almost) exclusively from the modification of the electrochemical response of the silane layer. The weak inhibitive effect shown by the small increase of the film resistance, R_f, evidences the formation of a more dielectric barrier film, that is evidenced by a decrease of one order of magnitude of the film capacitance. In this case, the reported corrosion protection characteristics induced by the addition of benzotriazole are found to be practically independent of the amount of compound added into the sol-gel procedure.

A greater enhancement of the corrosion protection skills of the silane layer was observed when Na-(diethyl(dithiocarbamate)) was added as inhibitor. In this case, the impedance parameters are found to depend strongly on the concentration of the inhibitor, the effect being especially noticeable on the film resistance, whereas the capacitance values remain in the same order of those produced in the presence of BTZ. By adding high quantities of DDTC to the sol-gel, the impedance response obtained was one order of magnitude higher than those obtained with MQ and LQ samples. Yet, high DDTC additions are needed to produce sufficient protection enhancement to AA2024-T3 alloy coated by the sol-gel procedure.

The highest inhibition efficiency was provided by adding Ce(III)-montmorillonite to the sol-gel coatings. A two-orders increase of the impedance modulus compared to BTZ- and DDTC-doped samples was obtained by adding 5 wt.% CeMMT, whereas rather moderate improvements, similar to those previously described for the other two inhibitors, occurred for MQ and LQ. It must be noticed that the 2-orders increased in the impedance values of CeMMT-HQ occurs also for both R_f and C_f. Therefore, it may be considered that the dielectric characteristics of the sol-gel coatings are mostly determined by the silane layer, and no major changes in the coating thickness are envisaged. Conversely, the changes operated by the inhibitor additions mostly influence the conductivity of the silane layer, probably by contributing to block the pores present in it, whereas the addition of CeMMT additionally modifies the reactivity at the metal/oxide interface, effectively reducing the oxidation rate of the alloy.

A remarkable corrosion protection was achieved when piperazine was added to the sol-gel coating. The addition of this compound to the silane layer originates a 3 orders of magnitude increase in the resistance values R_f compared to the control coating. From qualitative inspection of the impedance spectra, it was clear that the addition of the PIP resulted in the most protective ability of the sol-gel network. But this strong enhancement stems not only from the cross-linking abilities of the PIP, evidenced by the increase in the resistance of the system, but also contributes to the inhibition of the charge transfer process at the metal/oxide interface, especially at high contents of this compound.

Comparing the silane capacitance C_f and resistance R_f values listed on **Table 2** it can be observed that the second set of coatings (CeMMT-HQ, PIP-LQ and PIP-MQ) showed a C_f value one order of magnitude higher than the first set of coatings. This increase on the C_f value is due to an uptake of water, which is closely related to the first stage of a coating degradation. However, their R_f values are remarkably high. PIP-MQ reached a value of 2.2×10^6 Ω cm^2, while the value obtained for the control coating was of 19 Ω cm^2. The authors believe that there exists a degradation of the second set of coatings supported by the fact that a CPE was used instead of a capacitor for the silane film during the fit. The high R_f values obtained suggest that the inhibitors are being released and their activity is making the impedance modulus to increase. Similar behaviour was observed for PIP-HQ that presented the highest impedance and film resistance values.

3.2 Scanning electrochemical microscopy characterization: surface reactivity

The characterization of electrochemically active surfaces by SECM involves monitoring an electrochemical current with the UME tip. This faradaic response is originated by the electrochemical reaction of an electroactive species either placed in solution or evolving from the substrate. In this work, ferrocenemethanol was added to the chloride-containing test solution as redox mediator. Ferrocenemethanol, and its corresponding oxidized species, ferrocinium ion, are both soluble in the solution. The electrochemical reaction is highly reversible and involves the exchange of one electron. By setting the tip potential at +0.50 V vs. Ag/AgCl/KCl (3M), diffusion limiting conditions are ensured at the UME during the measurements. In these conditions, the current response of the tip when the UME is placed in the bulk solution is described by:

$$I_{t,\infty} = 4nFD_A C_A^* a \qquad (4)$$

where D_A and C_A^* are the diffusion coefficient and the bulk concentration of the redox mediator *A* in the bulk electrolyte solution, respectively; *n* is the number of electrons exchanged in the redox reaction, and *a* is the tip radius. This limiting current value, $I_{t,\infty}$, is taken for dividing and normalizing

the tip current response when the mediator interacts with the surface. That is, when the microelectrode tip is placed near a surface, the hemispherical condition for the diffusion-controlled transport of ferrocene-methanol is affected by the latter. That is, hindrance to diffusion should result in the presence of an electrochemically-inactive surface that effectively acts as an insulator, and the current measured at the tip must decrease with smaller tip-surface distances. This feature is usually named negative-feedback. A completely different condition occurs if the geometrically-blocking surface can provide the electrons required to regenerate ferrocene. In this case, though hindered diffusion still applies, the fast regeneration of the redox mediator at the electron-donor surface effectively acts as if an infinite source of electroactive species were placed near the microelectrode tip. As result, the faradaic current flowing through the tip increases with respect to the diffusion-limited value measured in the bulk of the electrolyte. Since electrons must be made available at the substrate/electrolyte interface for ferrocinium ions to be electroreduced back to ferrocene, this method allows to monitor, with high spatial resolution, either differences in surface conductivity of the layers formed on the substrate, that would correlate to chemical heterogeneities in the film, or to the presence of pores in which the electrolyte may get in contact with the buried metal surface. In the latter case, the metal/electrolyte interfaces originated inside the pores are the locations at which electrons would be supplied by the metal to the ferrocinium ion.

In a first set of experiments, two different regions were produced on the sol-gel coated samples by prior modification of a controlled portion of the coated metal surface by electrochemical processing. Namely, a cathodic polarization at -1.4 V vs. Ag/AgCl/KCl (3M) in 5 mM NaCl solution for 30 min was applied in order to test the adhesion characteristics and stability of the synthesized silane films, because at this negative potential the intermediate oxide layer formed on the metal will be reduced. As result, the dielectric characteristics of the intermediate alumina layer will disappear as electrically-conducting aluminium is obtained. After the cathodic polarization was applied to a portion of the surface, *Z*-approach curves were recorded at various locations arbitrarily chosen from each of the two regions developed on the coated metal surface. That is, the tip was approached towards sites taken in both the electrochemically-modified and the non-modified regions of the sample. Typical *Z*-approach curves measured at two locations from both regions on the non-doped (control) coating are depicted in **Figure 5**. It is observed that the curves measured over the non-modified region match the typical negative feedback behaviour expected for an insulating surface towards electron transfer. However, surface modification by cathodic polarization in the chloride solution resulted in a distinctive behaviour for the normalized current as the tip approaches the coated metal. Indeed, though hindered diffusion by an insulating surface dominates the current

response at the smallest tip-substrate distances, either the decrease from the bulk value $I_{t,\infty}$ is less abrupt than over the intact coating, or it even displays an intermediate region where normalized currents are somewhat bigger than unity (i.e, tip current values greater than the diffusion-limited value described by equation (4). This feature demonstrates the occurrence of a mixed positive-negative feedback response on the electrochemically-modified material. It arises from the electrochemical activation of the surface allowing regeneration of ferrocene-methanol to some extent. Thus, the electrochemical treatment produced on the portion of the coated substrate subjected to cathodic polarization at -1.4 V vs. Ag/AgCl/AgCl (3M) significantly enhanced the electrical conductivity of the material. The effect is more clearly evidenced by comparing the values of the normalized currents measured at the distance of closest approach that is taken as $Z = 0$. Accordingly, the values listed in **Table 3** allow a semi-quantitative estimation of the conductivity enhancement effect produced on the coated sample. The extent of this effect differs between the two sites arbitrarily chosen over the modified (pre-activated) region, thus evidencing heterogeneous activation of the sample during the electrochemical cathodic treatment. Though galvanic coupling between the two metallic areas with distinctive electrochemical behaviour cannot be completely discarded at this stage, yet the evidence of a very reproducible behaviour for the non-modified region, whereas there are differences between sites on the modified area, leads to the conclusion that electrochemical activity must occur at microgalvanic cells distributed along the pre-activated area, clearly more conductive in the whole than the unmodified silane coating.

The same procedure has been employed to characterize the silane coatings modified using corrosion inhibitors as shown in **Figure 6**. They depict the *Z*-approach curves measured for BTZ- and DDTC-containing layers, respectively. In each case, three different inhibitor concentrations were added to the sol-gel network, labelled LQ, MQ and HQ. From the inspection of Figures 6A-C, it is noted that the addition of BTZ produces the following effects: (1) an increase of the current values registered above the locations selected on the unmodified region of the BTZ-doped silane coating, resulting in similar responses to those obtained for the pre-activated region of the control sample (see Figure 5 for comparison); (2) the *Z*-approach curves cannot be superimposed in this case, evidencing heterogeneous behaviour of the BTZ-modified substrate even prior to the polarization procedure. It can thus be envisaged that the addition of BTZ to the sol-gel network may increase the substrate conductivity and/or its electron donation ability. This may stem from a less protective film, less compact as demonstrated with the EIS averaging measurements. Only the BTZ-HQ specimen seems to preserve the insulating characteristics of the silane film prior to the electrochemical modification procedure, most probably due to the larger resistance of the oxide layer formed on the metal, R_o,

which may be enough to hinder electron exchange with the ferrocenium species when it eventually reaches the metal/oxide interface through pores in the silane film. When approaching the SECM tip towards the electrochemically-modified region of the BTZ-modified substrates, the current values determined at a common relative distance from the substrate taken to be $Z = 0$ (cf. **Table 4**), are bigger than those measured above the unaltered region of the same sample. With the increase of BTZ content in the coating, this conductivity increase is still observed between polarized and non-polarized regions on the sample, though a direct dependence with BTZ content was not found, likewise it happened with EIS data analysis.

The *Z*-approach curves recorded on DDTC-modified systems, shown in Figures 6D-F, depict *Z*-approach curves that can be superimposed when registered over the non-polarized region of the sample, supporting the expectation of a more homogeneously-distributed surface activity before polarization. From the EIS analysis, the most relevant contribution in these systems compared to the other inhibitor (BTZ), was the bigger oxide resistance values obtained in the case of DDTC (cf. Table 2). Therefore, it can be deduced that, in the case of the addition of purely inhibitive compounds to the sol-gel matrix, the corrosion protection characteristics conferred to the coating by decreasing its pore distribution seem to be more determinant than the stress caused by the additions to the silane network and its adherence to the metal/oxide layer. Besides, polarized and non-polarized areas exhibit similar variations of the tip current with normalized distance for LQ and MQ systems, thus the polarization was not enough to decrease the sol-gel coating protection and to enhance its surface conductivity. Hence, DDTC seemed to play a key role towards corrosion protection when the sample experiences potentiostatic attack at low and medium additive ratios. This is in contrast with the situation encountered for the HQ system, where the sol-gel barrier apparently becomes partially degraded upon polarization with the result that the surface becomes more conductive, resulting in a greater contribution of the positive feedback. Indeed, from the minimum current data given in Table 4, the most insulating response was not obtained with the HQ system, as it might be expected, but for the MQ system. Not to avail, the MQ system presented bigger film and oxide capacitances at these apparently optimum conditions, while the oxide layer of the HQ system barely presents capacitive properties (cf. Table 2). This suggests again that species behaving as pure inhibitors mostly influence the surface conductivity and resistivity towards corrosive attack by altering the physicochemical characteristics of the silane film.

The SECM results obtained with the sol-gel coatings modified with Ce(III)-montmorillonite are shown in Figure 7A-C. Surprisingly, the most insulating and homogeneous behaviour was obtained with the LQ system, which also showed to be the less reactive after cathodic polarization.

However, the CeMMT-LQ system exhibited a behaviour very similar to that previously reported for BTZ-LQ when performing the EIS measurements, and poorly insulating properties were expected instead from SECM experiments. At present we cannot provide a satisfactory explanation for such contradictory result, though a chemical interaction between the CeMMT and the redox mediator cannot be discarded at this stage. Indeed, Ce(III) is a redox active species that may experience a direct charge transfer reaction with the ferrocene/ferrocenium system. In this case, MQ and HQ showed slightly higher tip-currents at the distance of closest approach in the Z-approach curves as observed in Table 4, and the stability of the sol-gel network was better and more homogeneous in the MQ case, as evidenced by the significant current increase seen for the HQ system. Thus, in spite of the greater resistance values obtained with the EIS measurements for the highest CeMMT content, the coatings does not remain stable after cathodic polarization.

Finally, the *Z*-approach curves measured in the case the cross-linking agent piperazine was added into the silane layer that are shown in Figure 7D-F, assisted to identify the potential action towards corrosion protection of this compound for the protection of AA2024-T3 aluminium alloy. Namely, no differences between polarized and non-polarized areas were appreciated for all the tested addition ratios, and a high insulating behaviour, which reached the expected values of the non-polarized area of the control coating, was obtained. This is in agreement with the very high R_o values determined from the analysis of the EIS data (cf. Table 2).

Immediately after completing the described SECM experiments, the coated aluminium alloy samples were removed from the solution, and their surface was imaged using an optical microscope leading. This led to the observation that all the substrates were clearly damaged other than the PIP-containing coated samples. In **Figure 8** the control sample, and the coatings with the lowest and highest insulating characteristics after polarization, respectively BTZ-HQ and PIP-HQ, are presented. This visual inspection was in good agreement with the conclusions derived from the SECM results; i.e., PIP showed the highest potential activity for corrosion protection of AA2024-T3 alloy.

It must be noticed that the *Z*-approach curves discussed above are the result of the electrochemical interaction of the sample with the redox mediator system added to the test electrolyte. That is, these plots specifically show the kinetic ability of the material towards the electron donation to that species. This effect has already been modelled for *Z*-approach curves measured over conductive substrates in SECM potentiometric operation, and the kinetic rate constant of the process can be calculated from comparison of an experimental curve with a set of theoretical plots [58]. As a prerequisite, the tip-substrate distance must be precisely known, that is, a *Z*-approach

curve over a surface presenting either null (i.e., insulating surface) or infinite kinetic constant must be observed in order to discern the intermediate cases. Unfortunately, this was not the case for all the recorded *Z*-approach curves presented in this work, since even the non-polarized areas showed, in most cases, certain degree of heterogeneity which gave rise to the occurrence of a partial positive feedback effect. For such estimation, we could only consider the control sample and the three less protective systems at the HQ situation, namely BTZ-HQ, DDTC-HQ and CeMMT-HQ. They all provide an apparently homogeneous insulating behaviour prior to cathodic polarization, which could be considered to be solely dependent on the negative feedback effect (i.e., kinetic constant tends to zero). Then, the subsequent cathodic polarization induced the activation of the coated surface (producing a finite kinetic constant). **Table 5** lists the calculated kinetic constant for these cases as determined using the mathematical procedure described in ref. [58], from which similar conclusions as those given in the semi-quantitative discussion can be extracted. The BTZ-doped system is again regarded to be the less stable system, while the addition of CeMMT provides the higher stability for the silane layer, even though lower quantities of CeMMT are apparently sufficient to maintain the surface insulating behaviour exclusively on the basis of the SECM *Z*-approach curves. However, care must be taken when considering these estimated values, as there is no guarantee that the non-polarized surfaces are actually electrically insulating, or rather they may present some degree of partial conductivity though homogeneously distributed over the surface.

In order to gain further insights on the surface activation process produced by applying a cathodic polarization to the coated aluminium alloy samples, the HQ systems were subjected to SECM area scans. In this way, eventual heterogeneities between the pre-activated and non-modified regions produced on the coated samples could be imaged in one experiment, thus aiming to confirm the heterogeneous response envisaged by the different trends found in the *Z*-approach curves. Results are given in **Figure 9** for the doped silane layers with the highest compound contents (i.e., the HQ systems), and with the control sample for comparison purposes. The pre-activated area was always located at the left side, although the presence of the boundary between polarized and non-polarized regions was not always easily distinguishable from the tip current maps. The control sample delivers the lowest tip-current response over the non-modified region and the greatest heterogeneity and activity over the polarized area (cf. Figure 9A). This is in accordance with the results given by the *Z*-approach curves given in Figure 5, where negative feedback resulted in rather small currents when approaching towards the non-polarized areas, and diverse activation rates over the previously polarized region.

Regarding the pure inhibitor systems, the BTZ-HQ system provides a heterogeneous response while scanning both areas, with smaller tip currents than those delivered by DDTC-HQ, that seems rather smooth in comparison (cf. Figures 9B and C). This agrees with the previous observation that the greater differences between the *Z*-approach curves registered over polarized and non-polarized regions occurred in the case of BTZ-HQ (see Figure 6C), while the polarization in the DDTC-HQ system did not induce significant surface activation. Regarding the other two compounds, the boundary between pre-activated and non-modified regions is better resolved in the case of the CeMMT-HQ system, reflecting a significant electrochemical activation of the surface in the two regions, in agreements with the observations derived from the analysis of the *Z*-approach curves (compare Figure 7C with Figure 9D). A more progressive variation between the two regions was observed in the SECM scan recorded for the PIP-HQ system (cf. Figure 9E), though smaller tip currents were recorded this time, mostly corresponding to a negative feedback effect. This, in conjunction with the impedance results, reflects the more insulating characteristics and greater stability of the piperazine-containing silane layer compared to the other systems thus resulting in a more protective sol-gel modified network. The more insulating characteristics of the PIP layers might account for the observation of a third time constant in the impedance spectra recorded at earlier exposures for the non-degraded film on AA2024-T3, for which the non-sealed surface layer model would not satisfactorily describe the system. Yet, at this stage it is still temptative to identify whether the enhanced corrosion protection effect produced by the addition of piperazine to the sol-gel treatment arises from blocking the pores typically formed in the silane layer, or by forming a more compact inner film directly in contact with the metal oxide layer spontaneously developed on the aluminium alloy. To our knowledge, the effect of piperazine to enhance the corrosion resistance of sol-gel films has not been reported until now, and a more detailed investigation of this system involving both electrochemical and surface analytical techniques would be required to unveil the source of this effect.

4. Conclusions

(1) The encapsulation of benzotriazole (BTZ) and Na-(diethyl(dithiocarbamate)) (DDTC) in the silane layer produces a weak enhancement of the corrosion protection of the aluminium alloy. The poorest performance is provided by BTZ.

(2) EIS data reveal that BTZ is unable to produce the blockage of the pores formed in the deposited layer. There is a high distribution of pores penetrating through the silane layer that may eventually expose the metal to the electrolyte.

(3) The inhibitive effect of DDTC was found to depend on the amount of compound employed. The corrosion protection operates on the resistance of the coating almost exclusively, thus indicating that the inhibitor must be effectively acting on the corrosion reaction inside the pores present in the silane layer.

(4) It was found by SECM that DDTC might operate with a passivating anodic mechanism, which is supported by the increase of electrochemical reactivity in the silane-coated substrate after applying a cathodic polarization step to the system.

(5) Further improvement of the corrosion resistance is obtained by using nanocontainers filled with Ce(III). An enhancement is observed in both the barrier characteristics of the silane layer and the insulating properties towards electron transfer in SECM. A mixed mechanism is observed, in which the dielectric characteristics of the silane layer are modified at the same time Ce(III) species can be released to heal the corroding sites developed inside the pores.

(6) Piperazine is regarded to be a very promising compound as it promotes both a less porous silane layer and an efficient inhibition of charge transfer reactions at the metal/oxide interface. This surface layer maintains its protective characteristics even when the intermediate metal oxide layer is electrochemically reduced.

(7) BTZ, DDTC and CeMMT are shown to provide inhibitor activity to sol-gel coatings, but the amounts required to provide sufficient inhibition efficiency for AA2024-T3 aluminium alloy in real applications have not yet been optimized.

Acknowledgements

The authors acknowledge the financial support from the Consejería de Educación de la Comunidad de Madrid (CAM, Madrid, Spain) through a MULTIMAT-CHALLENGE project (ref. S2013/MIT-2862), and from the Spanish Ministry of Economy and Competitiveness (MINECO, Madrid, Spain) and the European Regional Development Fund (Brussels, Belgium), under grants MAT2012/38650-C02-01 and CTQ2012-36787.

References

1. G.P. Bierwagen, D.E. Tallman, Choice and measurement of crucial aircraft coatings system properties, Progress in Organic Coatings 41 (2001) 201-216.
2. A. Boag, A.E. Hughes, N.C. Wilson, A. Torpy, C.M. MacRae, A.M. Glenn, T.H. Muster, How complex is the microstructure of AA2024-T3?, Corrosion Science 51 (2009) 1565-1568.

3. J.A. DeRose, T. Suter, A. Bałkowiec, J. Michalski, K.J. Kurzydlowski, P. Schmutz, Localised corrosion initiation and microstructural characterisation of an Al 2024 alloy with a higher Cu to Mg ratio, Corrosion Science 55 (2012) 313-325.
4. M. Sheffer, A. Groysman, D. Mandler, Electrodeposition of sol–gel films on Al for corrosion protection, Corrosion Science 45 (2003) 2893-2904.
5. D. Wang, G.P. Bierwagen, Sol–gel coatings on metals for corrosion protection, Progress in Organic Coatings 64 (2009) 327-338.
6. D. Raps, T. Hack, J. Wehr, M.L. Zheludkevich, A.C. Bastos, M.G.S. Ferreira, O. Nkuyen, Electrochemical study of inhibitor-containing organic–inorganic hybrid coatings on AA2024, Corrosion Science 51 (2009) 1012-1021.
7. A.A. El-Hadad, V. Barranco, A. Samaniego, I. Llorente, F.R. García-Galván, A. Jiménez-Morales, J.C. Galván, S. Feliu Jr., Influence of substrate composition on corrosion protection of sol–gel thin films on magnesium alloys in 0.6 M NaCl aqueous solution, Progress in Organic Coatings 77 (2014) 1642-1652.
8. T.G. Harvey, S.G. Hardin, A.E. Hughes, T.H. Muster, P.A. White, T.A. Markley, P.A. Corrigan, J. Mardel, S.J. Garcia, J.M.C. Mol, A.M. Glenn, The effect of inhibitor structure on the corrosion of AA2024 and AA7075, Corrosion Science 53 (2011) 2184-2190.
9. A. Ousslim, A.Chetouani , B. Hammouti, K. Bekkouch, S.S. Al-Deyab, A. Aouniti, A. Elidrissi, Thermodynamics, quantum and electrochemical studies of corrosion of iron by piperazine compounds in sulphuric acid, International Journal of Electrochemical Science 8 (2013) 5980-6004.
10. M.F. Montemor, D.V. Snihirova, M.G. Taryba, S.V. Lamaka, I.A. Kartsonakis, A.C. Balaskas, G.C. Kordas, J. Tedim, A. Kuznetsova, M.L. Zheludkevich, M.G.S. Ferreira, Evaluation of self-healing ability in protective coatings modified with combinations of layered double hydroxides and cerium molibdate nanocontainers filled with corrosion inhibitors, Electrochimica Acta 60 (2012) 31–40.
11. L. Paussa, F. Andreatta, D. De Felicis, E. Bemporad, L. Fedrizzi, Investigation of AA2024-T3 surfaces modified by cerium compounds: A localized approach, Corrosion Science 78 (2014) 376-386.
12. H.-Y. Su, P.-L. Chen, C.-S. Lin, Sol–gel coatings doped with organosilane and cerium to improve the properties of hot-dip galvanized steel, Corrosion Science 201 (2016) 63-71.

13. F. Mansfeld, M.W. Kendig, Electrochemical impedance tests for protective organic coatings, in: G. Haynes, R. Baboian (Eds.), Laboratory Corrosion Tests and Standards, ASTM STP 986, Philadelphia (PA), 1985, pp. 122-144.
14. R.L De Rosa, D.A Earl, G.P Bierwagen, Statistical evaluation of EIS and ENM data collected for monitoring corrosion barrier properties of organic coatings on Al-2024-T3, Corrosion Science 44 (2002) 1607-1620.
15. A.J. Bard, M.V. Mirkin (Eds.), Scanning Electrochemical Microscopy, 2nd. edition, CRC Press, Boca Raton (FL), 2012.
16. K. Mansikkamaki, P. Ahonen, G. Fabricius, L. Murtomaki, K. Kontturi, Inhibitive effect of benzotriazole on copper surfaces studied by SECM, Journal of The Electrochemical Society 152 (2005) B12-B16.
17. K. Mansikkamaki, U. Haapanen, C. Johans, K. Kontturi, M. Valden, Adsorption of benzotriazole on the surface of copper alloys studied by SECM and XPS, Journal of The Electrochemical Society 153 (2006) B311-B318.
18. J. Izquierdo, J.J. Santana, S. González, R.M. Souto, Uses of scanning electrochemical microscopy for the characterization of thin inhibitor films on reactive metals: the protection of copper surfaces by benzotriazole, Electrochimica Acta 55 (2010) 8791-8800.
19. M. Pähler, J.J. Santana, W. Schuhmann, R.M. Souto, Application of AC-SECM in Corrosion Science - Local visualisation of inhibitor films on active metals for corrosion protection, Chemistry A European Journal 17 (2011) 905-911.
20. J. Izquierdo, L. Nagy, J.J. Santana, G. Nagy, R.M. Souto, A novel microelectrochemical strategy for the study of corrosion inhibitors employing the scanning vibrating electrode technique and dual potentiometric/amperometric operation in scanning electrochemical microscopy: Application to the study of the cathodic inhibition by benzotriazole of the galvanic corrosion of copper coupled to iron, Electrochimica Acta 58 (2011) 707-716.
21. J. Izquierdo, J.J. Santana, S. González, R.M. Souto, Scanning microelectrochemical characterization of the anti-corrosion performance of inhibitor films formed by 2-mercaptobenzimidazole on copper, Progress in Organic Coatings 74 (2012) 526-533.
22. C. Li, L. Li, C. Wang, Y. Zhu, W. Zhang, Study of the protection performance of self-assembled monolayers on copper with the scanning electrochemical microscope, Corrosion Science 80 (2014) 511-516.

23. R.M. Souto, Y. González-García, S. González, G.T. Burstein, Damage to paint coatings caused by electrolyte immersion as observed *in situ* by scanning electrochemical microscopy, Corrosion Science 46 (2004) 2621-2628.
24. R.M. Souto, Y. González-García, S. González, In situ monitoring of electroactive species by using the scanning electrochemical microscope. Application to the investigation of degradation processes at defective coated metals, Corrosion Science 47 (2005) 3312-3323.
25. A.M. Simões, D. Battocchi, D.E. Tallman, G.P. Bierwagen, SVET and SECM imaging of cathodic protection of aluminium by a Mg-rich coating, Corrosion Science 49 (2007) 3838-3849.
26. R.M. Souto, Y. González-García, S. González, Characterization of coating systems by scanning electrochemical microscopy: surface topology and blistering, Progress in Organic Coatings 65 (2009) 435–439.
27. R.M. Souto, Y. González-García, J. Izquierdo, S. González, Examination of organic coatings on metallic substrates by scanning electrochemical microscopy in feedback mode: Revealing the early stages of coating breakdown in corrosive environments. Corrosion Science 52 (2010) 748-753.
28. S. González, J.J. Santana, Y. González-García, L. Fernández-Mérida, R.M. Souto, Scanning electrochemical microscopy for the investigation of localized degradation processes in coated metals: Effect of oxygen, Corrosion Science 53 (2011) 1910-1915.
29. M.B. Jensen, M.J. Peterson, N. Jadhav, V.J. Gelling, SECM investigation of corrosion inhibition by tungstate- and vanadate-doped polypyrrole/aluminum flake composite coatings on AA2024-T3, Progress in Organic Coatings 77 (2014) 2116-2122.
30. D.A. Walsh, L.E. Li, M.S. Bakare, K.T. Voisey, Visualisation of the local electrochemical activity of thermal sprayed anti-corrosion coatings using scanning electrochemical microscopy, Electrochimica Acta 54 (2009) 4647–4654.
31. D. Battistel, S. Daniele, G. Battaglin, M.A. Baldo, A simple electrochemical strategy for the characterisation of defects in alumina-coated metal substrates, Electrochemistry Communications 11 (2009) 2195–2198.
32. D. Battistel, S. Daniele, R. Gerbasi, M.A. Baldo, Characterization of metal-supported Al_2O_3 thin films by scanning electrochemical microscopy, Thin Solid Films 518 (2010) 3625–3631.
33. L. Johnson, A. Niaz, A. Boatwright, K.T. Voisey, D.A. Walsh, Scanning electrochemical microscopy at thermal sprayed anti-corrosion coatings: Effect of thermal spraying on heterogeneous electron transfer kinetics, Journal of Electroanalytical Chemistry 657 (2011) 46–53.

34. M.-Y. Jiang, L.-K. Wu, J.-M. Hu, J.-Q. Zhang, Silane-incorporated epoxy coatings on aluminum alloy (AA2024). Part 1: Improved corrosion performance, Corrosion Science 92 (2015) 118-126.
35. R.M. Souto, L. Fernández-Mérida, S. González, SECM imaging of interfacial processes in defective organic coatings applied on metallic substrates using oxygen as redox mediator, Electroanalysis 21 (2009) 2640-2646.
36. Y. Gonzalez-Garcia, J.M.C Mol, T. Muselle, I. De Graeve, G. Van Assche, G. Scheltjens, B. Van Mele, H. Terryn, SECM study of defect repair in self-healing polymer coatings on metals, Electrochemistry Communications 13 (2011) 169-173.
37. A. Pilbáth, T. Szabó, J. Telegdi, L. Nyikos, SECM study of steel corrosion under scratched microencapsulated epoxy resin, Progress in Organic Coatings 75 (2012) 480– 485.
38. M. Etienne, M. Dossot, J. Grausem, G. Herzog, Combined Raman microspectrometer and shearforce regulated SECM for corrosion and self-healing analysis, Analytical Chemistry 86 (2014) 11203−11210.
39. A.A. El Hadad, D. Carbonell, V. Barranco, A. Jiménez-Morales, B. Casal, J.C. Galván, Preparation of sol–gel hybrid materials from γ-methacryloxypropyltrimethoxysilane and tetramethyl orthosilicate: study of the hydrolysis and condensation reactions, Colloid and Polymer Science 289 (2011) 1875-1883.
40. Y. Ouyang, Y. Xie, S. Tan, Q. Shi, Y. Chen, Structure and antibacterial activity of Ce^{3+} exchanged montmorillonites, Journal of Rare Earths 27 (2009) 858-863.
41. C. Kranz, M. Ludwig, H.E. Gaub, W. Schuhmann, Lateral deposition of polypyrrole lines over insulating gaps. Towards the development of polymer-based electronic devices, Advanced Materials 7 (1995) 568-571.
42. F. Mansfeld, Analysis and interpretation of EIS data for metals and alloys, Technical Report 26, Solartron-Schlumberger, Farnborough, 1993, pp. 4.1-4.24.
43. M.-G. Olivier, M. Fedel, V. Sciamanna, C. Vandermiers, C. Motte, M. Poelman, F. Deflorian, Study of the effect of nanoclay incorporation on the rheological properties and corrosion protection by a silane layer, Progress in Organic Coatings 72 (2011) 15.
44. S.A.S. Dias, S.V. Lamaka, C.A. Nogueira, T.C. Diamantino, M.G.S. Ferreira, Sol–gel coatings modified with zeolite fillers for active corrosion protection of AA2024, Corrosion Science 62 (2012) 153-162.
45. I.A. Kartsonakis, E. Athanasopoulou, D. Snihirova, B. Martins, M.A. Koklioti, M.F. Montemor, G. Kordas, C.A. Charitidis, Multifunctional epoxy coatings combining a mixture of traps and

inhibitor loaded nanocontainers for corrosion protection of AA2024-T3, Corrosion Science 85 (2014) 147-159.

46. V. Dalmoro, J.H.Z. dos Santos, C. Alemán, D.S. Azambuja, An assessment of the corrosion protection of AA2024-T3 treated with vinyltrimethoxysilane/(3-glycidyloxypropyl)trimethoxysilane, Corrosion Science 92 (2015) 200-208.
47. J.R. Macdonald, Note on the parameterization of the constant-phase admittance element, Solid State Ionics 13 (1984) 147-149.
48. A. Perrotta, S.J. García, M. Creatore, Ellipsometric Porosimetry and electrochemical Impedance Spectroscopy Characterization for Moisture Permeation Barrier Layers, Plasma Process. Polym. 2015, 12, 968–979.
49. D. Zhu, W.J. van Ooij, Corrosion protection of AA 2024-T3 by bis-[3-(triethoxysilyl)propyl]tetrasulfide in sodium chloride solution.: Part 2: mechanism for corrosion protection, Corrosion Science 45 (2003) 2177-2197.
50. P. Campestrini, H. Terryn, J. Vereecken, J.H.W. de Wit, Chromate conversion coating on aluminum alloys: III. Corrosion protection, Journal of The Electrochemical Society 151 (2004) B370-B377.
51. M.L. Zheludkevich, R. Serra, M.F. Montemor, I.M. Miranda Salvado, M.G.S. Ferreira, Corrosion protective properties of nanostructured sol–gel hybrid coatings to AA2024-T3, Surface and Coatings Technology 200 (2006) 3084-3094.
52. S.A.S. Dias, S.V. Lamaka, C.A. Nogueira, T.C. Diamantino, M.G.S. Ferreira, Sol-gel coatings modified wit zeollite fillers for active corrosion protection of AA2024, Corrosion Science 62 (2012) 153-162.
53. V. Dalmoro, J.H.Z. dos Santos, C. Alemán. D.S. Azambuja, An assessment of the corrosion protection of AA2024-T3 treated with vinyltrimethoxysilane/(3-glycidyloxypropyl)trimethoxysilane, Corrosion Science 92 (2015) 200-208.
54. X. Yuan, Z.F. Yue, X. Chen, S.F. Wen, L. Li, T. Feng, The protective and adhesion properties of silicone-epoxy hybrid coatings on 2024 Al-alloy with a silane film as pre-treatment, Corrosion Science 104 (2016) 84-97.
55. G.X. Shen, Y.C. Shen, C.J. Lin, Corrosion protection of 316 L stainless steel by a TiO2 nanoparticle coating prepared by sol-gel method, Thin Solid Films 489 (2005) 130-136.
56. J. Lausmaa, B. Kasemo, H. Mattson, H. Odelius, Multitechnique surface characterization of oxide-films on electropolished and anodically oxidized titanium, Applied Surface Science 45 (1990) 189-200.

57. J. Pan, D. Thierry, C. Leygraf, Electrochemical and XPS studies of titanium for biomaterial applications with respect to the effect of hydrogen peroxide, Journal of Biomedical Materials Research 28 (1994) 113-122.
58. R. Cornut, C. Lefrou, New analytical approximation of feedback approach curves with a microdisk SECM tip and irreversible kinetic reaction at the substrate, Journal of Electroanalytical Chemistry 621 (2008) 178-184.

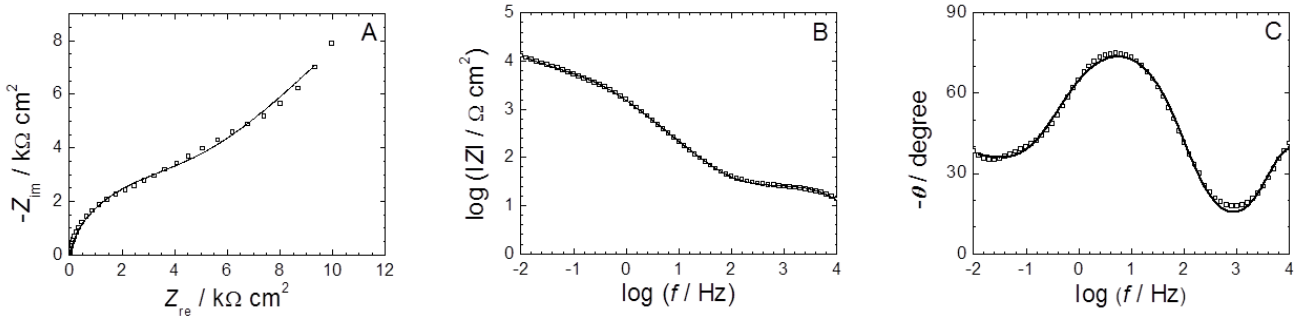

Figure 1. Measured (discrete points) and fitted (solid lines) impedance spectrum of AA2024-T3 aluminium alloy coated with the control (undoped) silane layer after 72 h exposure to aerated 0.05 M NaCl solution.

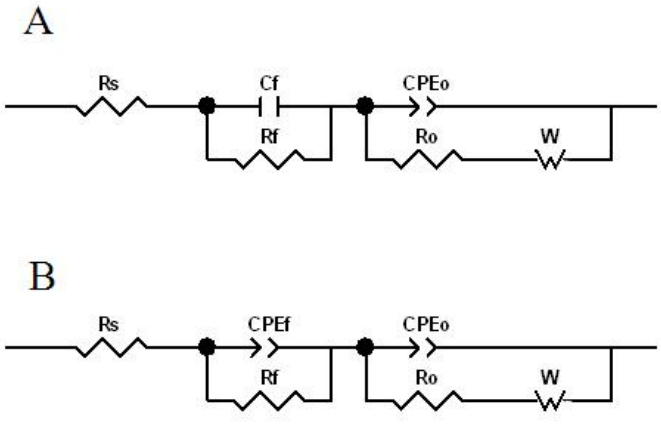

Figure 2. Equivalent circuits (EC) used to model the impedance data.

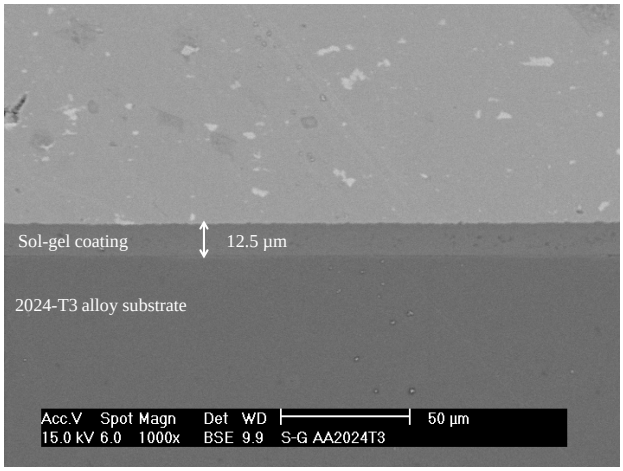

Figure 3. Micrograph obtained with a scanning electron microscope on the cross section of the control sol-gel coating applied on AA2024-T3 aluminium alloy.

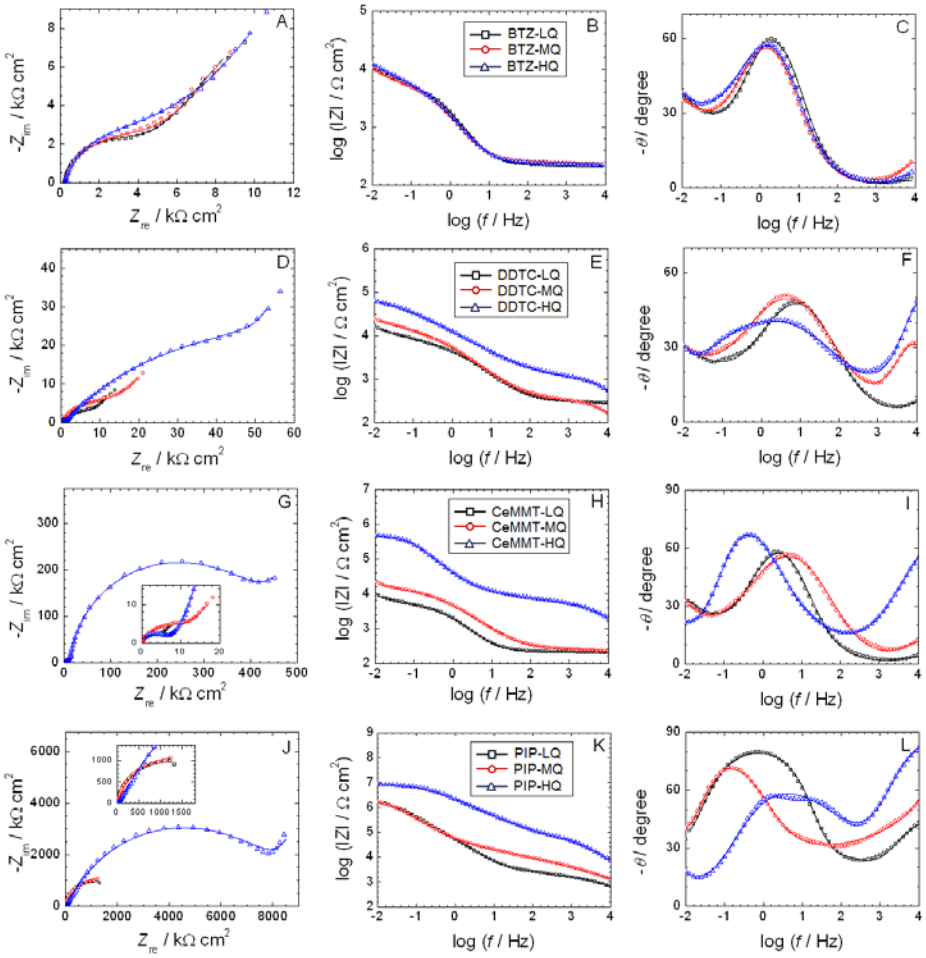

Figure 4. Measured (discrete points) and fitted (solid lines) impedance spectra of AA2024-T3 aluminium alloy substrates coated with doped silane layers after 72 h exposure to aerated 0.05 M NaCl solution. The additives and their concentration ratios are indicated in the graphs.

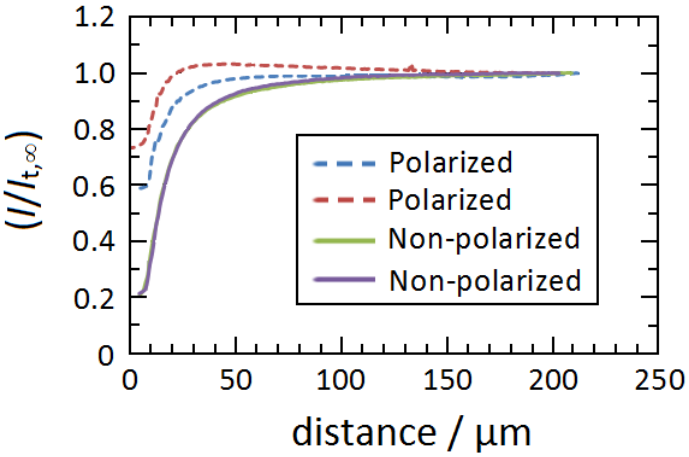

Figure 5. SECM normalized *Z*-approach curves towards a control (non-doped) silane-coated AA2024-T3 aluminium surface measured in 5 mM NaCl + 0.5 mM ferrocenemethanol solution. A portion of the exposed silane-coated surface was electrochemically modified by applying a cathodic polarization at -1.4 V vs. Ag/AgCl/KCl (3M) for 30 min during exposure to 5 mM NaCl solution. This electrochemical modification procedure was performed prior to solution replacement by the ferrocenemethanol-containing solution required to record the *Z*-approach curves. Two approach curves were measured over locations arbitrarily chosen on the electrochemically-modified surface, and the other two were taken over locations on the unmodified silane layer. Tip potential: +0.50 V vs. Ag/AgCl/KCl (3M).

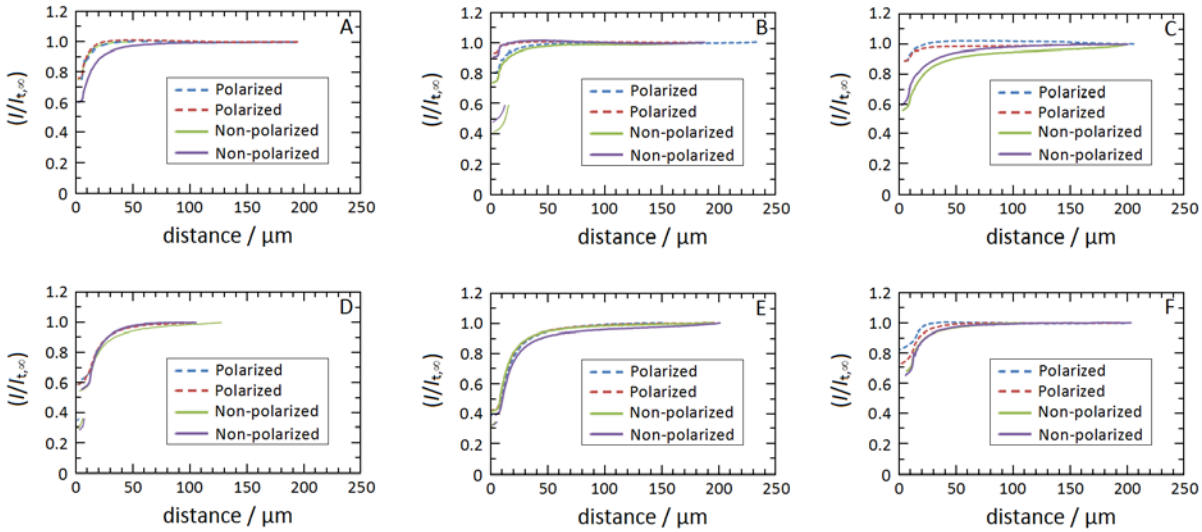

Figure 6. SECM normalized *Z*-approach curves towards AA2024-T3 aluminium alloys coated with inhibitor-doped silane layers measured in 5 mM NaCl + 0.5 mM ferrocenemethanol solution. Added inhibitors: (A-C) benzotriazole (BTZ), and (D-F) Na-(diethyl(dithiocarbamate)) (DDCT); three different inhibitor concentration ratios were employed in each case as listed in Table 1, namely: (A,D) Low, (B,E) Medium, and (C,F) High. A portion of the exposed silane-coated surface was electrochemically modified by applying cathodic polarization at -1.4 V vs. Ag/AgCl/KCl (3M) for 30 min while exposed to 5 mM NaCl solution. This electrochemical modification procedure was performed prior to solution replacement by the ferrocenemethanol-containing solution required to record the *Z*-approach curves. Two approach curves were measured over locations arbitrarily chosen on the electrochemically-modified surface, and the other two were taken over locations on the unmodified silane layer. Tip potential: +0.50 V vs. Ag/AgCl/KCl (3M).

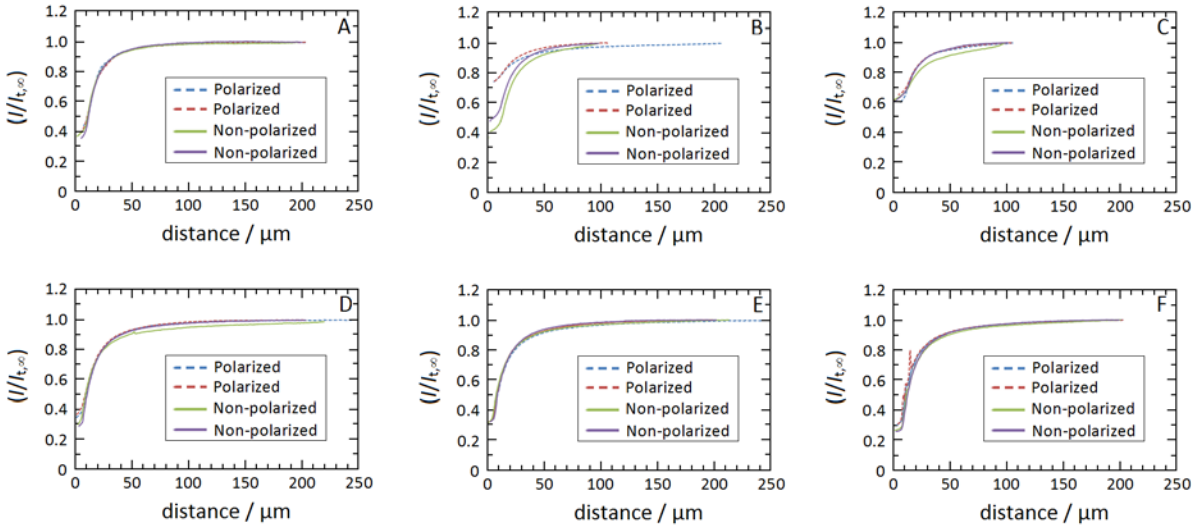

Figure 7. SECM normalized *Z*-approach curves towards AA2024-T3 aluminium alloys coated with silane layers containing either (A-C) piperazine as cross-linking agent, or (D-F) Ce(III)-montmorillonite as mixed barrier and inhibitor system; three different concentration ratios of the additives were employed in each case as listed in Table 1, namely: (A,D) Low, (B,E) Medium, and (C,F) High. They were measured in 5 mM NaCl + 0.5 mM ferrocenemethanol solution. A portion of the exposed silane-coated surface was electrochemically modified by applying cathodic polarization at -1.4 V vs. Ag/AgCl/KCl (3M) for 30 min while exposed to 5 mM NaCl solution. This electrochemical modification procedure was performed prior to solution replacement by the ferrocenemethanol-containing solution required to record the *Z*-approach curves. Two approach curves were measured over locations arbitrarily chosen on the electrochemically-modified surface, and the other two were taken over locations on the unmodified silane layer. Tip potential: +0.50 V vs. Ag/AgCl/KCl (3M).

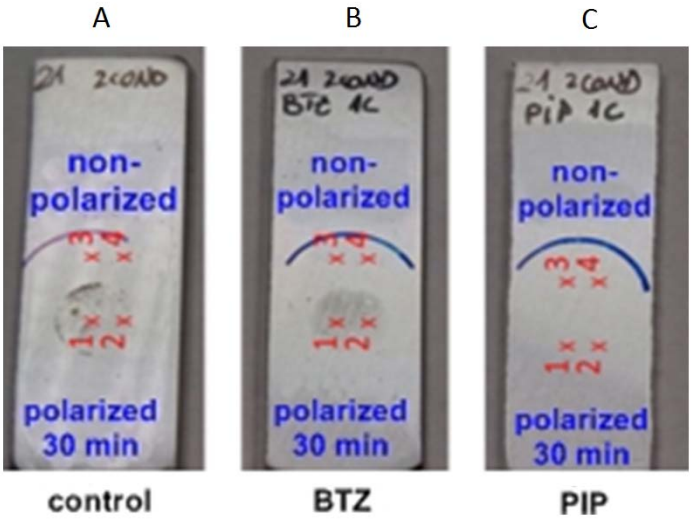

Figure 8. Optical photographs of sol-gel coated AA2024-T3 substrates after SECM characterization in 5 mM NaCl + 0.5 M ferrocene-methanol. Composition of the silane layers: (A) control (undoped), (B) BTZ HQ, and (C) PIP HQ. They images exhibit the two regions produced on the samples resulting from applying cathodic polarization at -1.4 V vs. Ag/AgCl/KCl (3M) to the lower half of the sample. They also exhibit a circular area at the center that was limited by the o-ring employed to confine the test electrolyte in the SECM cell arrangement.

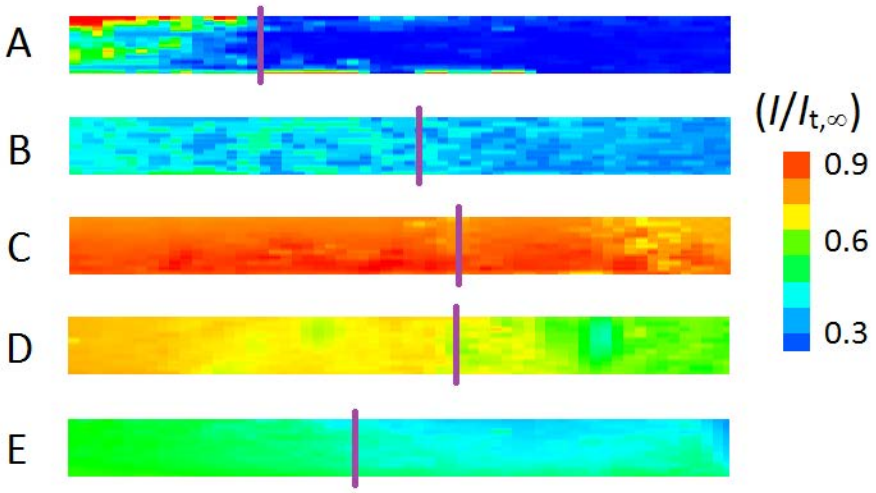

Figure 9. Images generated by SECM of silane-coated AA2024-T3 surfaces with different zones, corresponding to prior electrochemical modification at -1.4 V vs. Ag/AgCl/KCl (3M) for 30 min (left) and non-modified (right). The approximate boundary between the two zones is indicated by a vertical line in each image. (A) Control (undoped) silane layer, (B) BTZ HQ, (C) DDTC HQ, (D) Ce-MMT HQ, and (E) PIP HQ. The samples were immersed in 5 mM NaCl + 0.5 ferrocenemethanol solution. Tip-substrate distance: 15 µm. Tip potential: +0.50 V vs. Ag/AgCl/KCl (3M). The *Z* scale is the normalized tip current ($I/I_{t,\infty}$). The sample was left at its spontaneous open circuit potential in the electrolyte.

Table 1. Composition of the silane layers used in this study. Compositions are given in water:component molar ratio for the inhibitors, and in wt.% for Ce(III)-montmorillonite.

Sample	Component	Water:component / Molar ratio	Wt.% of component
Control	-	-	-
BTZ LQ	BTZ	1/1000	-
BTZ MQ		1/500	
BTZ HQ		1/100	
DDTC LQ	DDTC	1/1000	-
DDTC MQ		1/500	
DDTC HQ		1/100	
CeMMT LQ	Ce(III)-MMT	-	1
CeMMT MQ			3
CeMMT HQ			5
PIP LQ	Piperazine	1/1000	-
PIP MQ		1/500	
PIP HQ		1/100	

Table 2. Parameters of the equivalent circuit for silane-coated AA2024-T3 alloys immersed in 0.05 M NaCl for 72 h. AC polarization was applied around their corresponding open circuit potential values in the electrolyte.

Impedance parameters	Sample												
	Control	BTZ			DDTC			CeMMT			PIP		
		LQ	MQ	HQ	LQ	MQ	HQ	LQ	MQ	HQ	LQ	MQ	HQ
	1st set of coatings									2nd set of coatings			
OCP $_{1\ hour}$ / mV vs. Ag/AgCl/KCl (3M)	-520	-527	-517	-523	-524	-578	-525	-521	-535	-538	-557	-476	-497
OCP $_{72\ hours}$ / mV vs. Ag/AgCl/KCl (3M)	-540	-567	-563	-555	-569	-555	-566	-555	-544	-580	-512	-536	-506
log $\|Z\|_{LF}$	4.104	4.031	4.013	4.096	4.209	4.393	4.819	3.972	4.337	5.687	6.205	6.209	6.949
R_f / Ω cm^2	19.0	21.5	76.6	43.7	70.1	200.7	785.1	26.6	78.9	$3.7\cdot10^5$	$2.1\cdot10^5$	$2.2\cdot10^6$	$6.4\cdot10^6$
C_f / µF cm^{-2}	1.62	0.900	0.162	0.304	0.163	0.177	0.041	0.555	0.201	5.602	3.597	4.346	1.110
n_f	--	--	--	--	--	--	--	--	--	0.987	0.923	0.929	0.859
R_o / kΩ cm^2	4.67	4.34	4.74	5.14	6.50	1.46	95.1	4.25	12.0	5.3	3.2	44.4	109
C_o / µF cm^{-2}	111	75.7	102.5	99.6	37.3	42.8	28.7	87.4	43.5	0.05	4.7	7.6	6.4
n_o	0.906	0.915	0.878	0.872	0.746	0.700	0.538	0.892	0.776	0.816	0.478	0.371	--
C_3 / µF cm^{-2}	--	--	--	--	--	--	--	--	--	--	--	--	0.002
R_3 / kΩ cm^2	--	--	--	--	--	--	--	--	--	--	--	--	43.2

Table 3. Normalized current values measured when the SECM tip was placed at the point of closest approach to the surface (taken as $Z = 0$) determined from the Z-approach curves measured for a control (non-doped) silane coating applied on AA2024-T3 alloy sample during immersion in 5 mM NaCl + 0.5 mM ferrocenemethanol solution that are shown in Figure 4. A portion of the exposed silane-coated surface was electrochemically modified by applying a cathodic polarization at -1.4 V vs. Ag/AgCl/KCl (3M) for 30 min during exposure to 5 mM NaCl solution. This electrochemical modification procedure was performed prior to solution replacement by the ferrocenemethanol-containing solution required to record the Z-approach curves. Two approach curves were measured over locations arbitrarily chosen on the electrochemically-modified surface, and the other two were taken over locations on the unmodified silane layer.

Sample	Region	$(I / I_{t,\infty})$
Control	Non-polarized	0.281
		0.264
	Polarized	0.604
		0.777

Table 4. Normalized current values measured when the SECM tip was placed at the point of closest approach to the surface (taken as $Z = 0$) determined from the *Z*-approach curves measured for doped silane layers applied on AA2024-T3 alloys samples during immersion in 5 mM NaCl + 0.5 mM ferrocenemethanol solution that are shown in Figures 5 and 6. A portion of the exposed silane-coated surface was electrochemically modified by applying a cathodic polarization at -1.4 V vs. Ag/AgCl/KCl (3M) for 30 min during exposure to 5 mM NaCl solution. This electrochemical modification procedure was performed prior to solution replacement by the ferrocenemethanol-containing solution required to record the *Z*-approach curves. Two approach curves were measured over locations arbitrarily chosen on the electrochemically-modified surface, and the other two were taken over locations on the unmodified silane layer.

		$(I / I_{t,\infty})$			
Sample	**Region**	**Component**			
		BTZ	**DDTC**	**Ce-MMT**	**PIP**
LQ	Non-polarized	0.764	0.617	0.469	0.375
		0.593	0.617	0.435	0.302
	Polarized	0.766	0.670	0.479	0.391
		0.767	0.685	0.484	0.415
MQ	Non-polarized	0.759	0.463	0.497	0.418
		0.915	0.410	0.593	0.354
	Polarized	0.814	0.415	0.791	0.365
		0.939	0.466	0.792	0.389
HQ	Non-polarized	0.598	0.761	0.686	0.291
		0.663	0.706	0.688	0.282
	Polarized	0.908	0.874	0.683	0.341
		0.900	0.802	0.708	0.383

Table 5. Kinetic constant rate values, *k*, for electron transfer from/to the substrate for undoped and HQ-doped silane layers applied on AA2024-T3 aluminium alloy by a sol-gel technique. They have been determined by fitting measured SECM *Z*-approach curves measured above the region subjected to cathodic polarization (2 curves in each case) to a set of theoretical curves [38].

		Sample			
		Control	**BTZ-HQ**	**DDTC-HQ**	**CeMMT-HQ**
k / cm s^{-1}	**# 1**	5.77×10^{-4}	1.54×10^{-3}	1.020^{-3}	3.64×10^{-4}
	# 2	1.86×10^{-3}	1.18×10^{-3}	4.11×10^{-4}	4.57×10^{-4}